Observation and control of hybrid spin-wave-Meissner-current transport modes

Borst, M.; Vree, P. H.; Lowther, A.; Teepe, A.; Kurdi, S.; Bertelli, I.; Simon, B. G.; Blanter, Y. M.; van der Sar, T.

DOI
10.1126/science.adj7576

Publication date
2023

Document Version
Final published version

Published in
Science (New York, N.Y.)

SPINTRONICS

Observation and control of hybrid spin-wave–Meissner-current transport modes

M. Borst, P. H. Vree, A. Lowther, A. Teepe, S. Kurdi, I. Bertelli, B. G. Simon, Y. M. Blanter, T. van der Sar*

Superconductors are materials with zero electrical resistivity and the ability to expel magnetic fields, which is known as the Meissner effect. Their dissipationless diamagnetic response is central to magnetic levitation and circuits such as quantum interference devices. In this work, we used superconducting diamagnetism to shape the magnetic environment governing the transport of spin waves—collective spin excitations in magnets that are promising on-chip signal carriers—in a thin-film magnet. Using diamond-based magnetic imaging, we observed hybridized spin-wave–Meissner-current transport modes with strongly altered, temperature-tunable wavelengths and then demonstrated local control of spin-wave refraction using a focused laser. Our results demonstrate the versatility of superconductor-manipulated spin-wave transport and have potential applications in spin-wave gratings, filters, crystals, and cavities.

The ability to control the transport of spins and charges with metal electrodes is fundamental to information-processing devices and an indispensable tool in quantum and condensed-matter physics. Although devices such as spin valves and transistors are based on the transport of uncorrelated particles (*1*), the excitations of magnetic materials, known as spin waves, are emerging as promising alternative information carriers (*2*). These collective spin excitations provide new opportunities for realizing analog or binary device functionality based on their wave nature, nonreciprocal transport properties, and low intrinsic damping (*3*).

Control of spin-wave transport is possible by heavy-metal electrodes that enable modulation by means of the spin-Hall effect (*4*–*6*) or by auxiliary magnetic materials that modify the spin-wave spectrum (*7*, *8*). However, metallic gates can also introduce additional spin-wave damping because of uncontrolled spin pumping or spin-wave–induced eddy currents (*6*, *9*, *10*). Furthermore, the diamagnetic response of normal metals is dominated by ohmic resistance, precluding effective stray-field control of the spin-wave spectrum.

An attractive approach for strong, low-damping spin-wave modulation is to use superconducting electrodes. Superconductors are materials with zero electrical resistivity and a strong diamagnetic response that enables the creation of magnetic shields, magnetic lenses, and circuits such as quantum bits and quantum interference devices (*11*, *12*). Spin-wave spectroscopy measurements have demonstrated that superconducting strips on magnetic films can alter the spin-wave spectrum through the backaction of induced currents (*13*) or the interaction with Abrikosov vortices (*14*). Recently, it was proposed to harness the diamagnetism of a superconductor to create the spin-wave equivalents of optical mirrors and cavities (*15*). Being able to image and control spin waves as they travel underneath superconducting electrodes would enable insight into the nature of the spin wave–superconductor interaction and unlock opportunities to control the propagation, dispersion, and refraction of spin waves.

In this work, we developed, imaged, and studied temperature-, field-, and laser-tunable spin-wave transport enabled by a superconducting strip on a thin-film magnetic insulator (Fig. 1A). We used magnetic resonance imaging based on nitrogen-vacancy (NV) spins in diamond (*16*–*18*) to study the spin waves as they travelled underneath the optically opaque superconductor.

Imaging hybrid spin-wave–Meissner-current transport modes using spins in diamond

Our system consisted of a thin film of yttrium iron garnet (YIG), a magnetic insulator with low spin-wave damping (*2*), equipped with gold microstrips for spin-wave excitation and a molybdenum-rhenium superconducting strip for spin-wave modulation (Fig. 1A). To image the spin waves, we placed a diamond membrane that contained a thin layer of NV sensor spins on top of the sample (Fig. 1A and fig. S1) (*18, 19*). These spins detect the spin waves by their microwave magnetic stray fields, which enables imaging through optically opaque materials (*10*). The sample was embedded in a variable temperature cryostat with a base temperature of 5.5 K and free-space optical access to read out the NV sensor spins.

NV centers are atomic defects in the diamond carbon lattice with an $S = 1$ electron spin (*16*). The sensitivity of the NV spin to magnetic fields, combined with its optical spin readout and excellent spin coherence, has enabled widespread sensing applications in fi ranging from condensed-matter science to ology and biophysics (*20*–*22*). Here we used the sensitivity of the NV spins to microwave magnetic fields to image the spin waves in our YIG film (*17*, *18*, *23*, *24*). When resonant with an NV electron spin resonance (ESR) frequency, the stray field of the spin waves drives transitions between the NV spin states, which we detected through the spin-dependent NV photoluminescence under green-laser excitation.

We applied a magnetic bias field to tune the NV ESR frequency into resonance with spin waves of different spin wavelengths (Fig. 1B). By orienting the field along one of the four possible crystallographic NV orientations (Fig. 1A), we split the ESR frequency of this "field-aligned" NV ensemble (f_1) off from that of the three other NV ensembles (f_2) as shown in the optically detected resonance spectrum of Fig. 1C. Alternatively, we applied the field in plane along $\hat{\boldsymbol{z}}$ to enable measurements at different frequencies at a given magnetic field. Because the applied magnetic fields are much smaller than the YIG saturation magnetization, the YIG magnetization lies predominantly in-plane along $\hat{\boldsymbol{z}}$ for both field orientations (Damon-Eshbach geometry).

To demonstrate the spin-wave modulation capabilities of our superconductor, we imaged the spin-wave transport above and below the molybdenum-rhenium (MoRe) superconducting transition temperature $T_c = 8.7$ K (Fig. 2, A to D). We generated NV-resonant spin waves with wavevector $\boldsymbol{k} = k\hat{\boldsymbol{y}}$ by applying a microwave current at NV frequency f_1 to the gold microstrip located just left outside of the imaging area. The interference between the microwave magnetic stray field generated by these spin waves and the direct microstrip field leads to a spatial standing-wave modulation of the NV ESR contrast (*17*, *18*). Crucial for our measurements, this interference effect enables a straightforward extraction of the spin wavelength. The spatial map of the ESR contrast C_1 at $T = 10.7$ K (above T_c) shows spin waves traveling toward and then underneath the MoRe strip without a change in wavelength (Fig. 2B). By contrast, the spin-wavelength increased almost twofold when the strip was cooled into its superconducting state at $T = 5.5$ K (Fig. 2C). Averaging the maps along $\hat{\boldsymbol{z}}$ (Fig. 2E) highlights the spatial homogeneity of the wavelength change.

We explained the superconductor-induced change of the spin wavelength by developing an analytical expression for the spin-wave dispersion in a magnet-superconductor thin-film hybrid. In this model, building on the formalism developed in (*15*), the spin waves induce AC Meissner currents that are governed by the London penetration depth λ_L of the superconductor. These currents, in turn, generate a magnetic field that acts back on the spin waves.

Department of Quantum Nanoscience, Kavli Institute of Nanoscience, Delft University of Technology, 2628 CJ Delft, Netherlands.
*Corresponding author. Email: t.vandersar@tudelft.nl

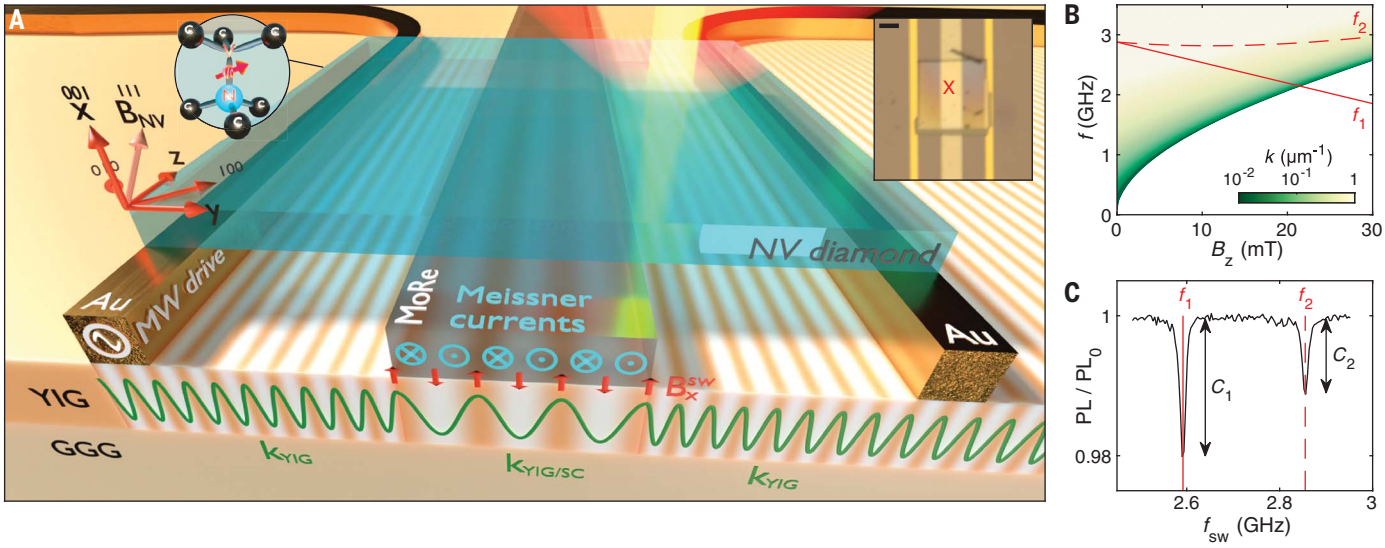

Fig. 1. Magnetic resonance imaging of hybridized spin-wave–Meissner-current transport modes. (**A**) Overview of the experiment. A gold (Au) microstrip excites spin waves with wavevector $\boldsymbol{k} = k\hat{\boldsymbol{y}}$ in a 245-nm-thick film of yttrium iron garnet (YIG). The spin waves travel toward a molybdenum rhenium (MoRe) superconducting strip (width W = 30 μm, thickness t = 140 nm) where their stray fields induce Meissner currents that act back on the spin waves, shifting their wave number to $k_{YIG/SC} < k_{YIG}$ (SC, superconductor). We imaged the waves underneath and next to the superconductor by their microwave magnetic stray fields using a ~20-nm-thick layer of nitrogen-vacancy (NV) spins implanted at ~0.07 μm below the bottom surface of a 100 × 100 × 5 μm^3 diamond membrane placed on top of the sample. A magnetic field $\boldsymbol{B}_{NV} = B_x\hat{\boldsymbol{x}} + B_z\hat{\boldsymbol{z}}$ applied at θ = 54° with respect to the x axis yields an in-plane YIG magnetization along $\hat{\boldsymbol{z}}$ for the small fields applied and directional Damon-Eshbach spin-wave excitation. GGG, gadolinium gallium garnet, SW, spin wave. (Inset) Optical micrograph of NV diamond and Au and MoRe strips on the YIG. Scale bar, 30 μm. Au thickness, 200 nm. (**B**) YIG dispersion (color map) and NV electron spin resonance (ESR) frequencies (red lines) as a function of the in-plane field component $B_z = B_{NV}\cos\theta$. f_1 and f_2 denote the ESR frequencies of NV spins with zero-field quantization axis aligned or misaligned with $\boldsymbol{B}_{NV}$, respectively. The intersection of the ESR frequencies with the spin-wave dispersion sets the detectable spin-wave numbers k. (**C**) Optically detected NV ESR spectrum at B_z = 10 mT, at a location denoted by the red cross in the inset of (A). The ESR contrast C_1 or C_2, where the subscript identifies the field-aligned or misaligned NV ensemble, respectively, results from interference between the microstrip field and spin-wave field, enabling spatial mapping of the spin-wave fronts.

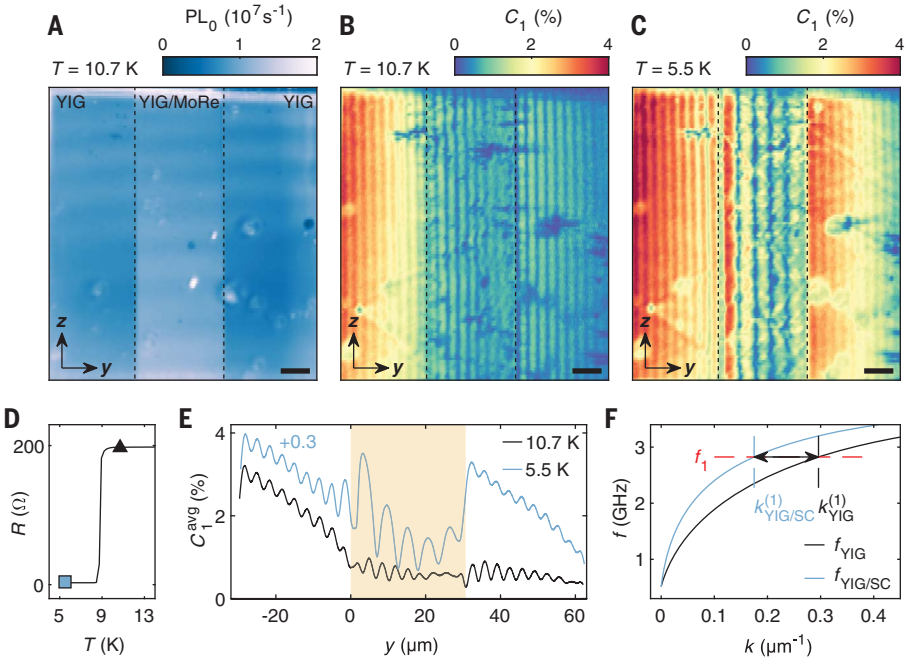

Fig. 2. Magnetic resonance imaging of spin waves above and below the superconducting transition temperature. (**A**) Spatial map of the NV photoluminescence PL_0 in the absence of microwaves, showing the MoRe strip (between the vertical dashes). Scale bar, 10 μm. (**B** and **C**) Spatial maps of the NV electron spin resonance contrast C_1 above (B) and below (C) the superconducting transition temperature of T_c = 8.7 K at T = 10.7 and 5.5 K, respectively. The Au, which excites spin waves, is located just outside the left edge of the imaged area. Above T_c, the wavelength is unaffected by the MoRe strip; below T_c, it is lengthened. (**D**) DC resistance R of the MoRe strip as a function of temperature T, with markers indicating the resistance of the film during the measurements of (B) triangle and (C) square. (**E**) Data from (B) and (C) averaged over the z direction, with the MoRe strip indicated by yellow shading. (**F**) Calculated spin-wave dispersion $f_{YIG}(k)$ for bare YIG, and $f_{YIG/SC}(k, \lambda_L)$ for YIG, covered by a superconducting film with London penetration depth λ_L = 400 nm. The superconductor shifts the dispersion upwards by $f_{SC}(k, \lambda_L)$, which manifests as a reduction in the wave number at NV frequency f_1 from $k_{YIG}^{(1)}$ to $k_{YIG/SC}^{(1)}$, indicated by the dashed lines.

By integrating this field self-consistently into the Landau-Lifshitz-Gilbert equation, we found that the spin-wave dispersion shifts upwards in frequency as

$$f_{\mathrm{YIG/SC}}(k,\lambda_L) = f_{\mathrm{YIG}}(k) + f_{\mathrm{SC}}(k,\lambda_L) \quad (1)$$

where $f_{\mathrm{YIG}}(k)$ is the bare-YIG spin-wave dispersion (SI) and

$$f_{\mathrm{SC}}(k,\lambda_L) \approx \gamma\mu_0 M_s k t r \frac{1-e^{-2h/\lambda_L}}{(k\lambda_L+1)^2-(k\lambda_L-1)^2 e^{-2h/\lambda_L}} \quad (2)$$

is the superconductor-induced shift [supplementary text, section S1 (*19*)]. Here, M_s is the YIG saturation magnetization, t = 245 nm is the YIG thickness, h = 140 nm is the superconductor thickness, γ = 28 GHz/T is the electron gyromagnetic ratio, μ_0 is the vacuum permeability, and r is a dimensionless factor associated with the YIG thickness and spin-wave ellipticity. The approximation holds when the kinetic inductance dominates the impedance, as is the case for our superconducting strip [supplementary text, section S1 (*19*)], and when $k^2\lambda_L^2 \ll 1$. A more general expression is given in the supplementary text (*19*). The dispersion shift $f_{SC}(k,\lambda_L)$ is maximal when $\lambda_L \to 0$, in which case the superconductor perfectly screens the spin-wave stray field. This limit was analyzed in (*25*, *26*) by considering a magnetic film covered by a "perfect metal" as defined by a perfect magnetic field screening. Indeed, when we let $\lambda_L \to 0$, the shift calculated by our model approached the shift predicted in (*19*, *25*, *26*). The calculated bare YIG and hybridized YIG-MoRe spin-wave dispersions are compared in Fig. 2F. The upwards frequency shift underneath the superconductor manifested as a reduction in wave number of the NV-resonant spin waves detected in our experiments (Fig. 2E).

We observed that the ESR contrast just to the right of the MoRe strip was higher than that in the MoRe-strip region (Fig. 2C), consistent with the screening of the spin-wave field by the Meissner currents. In addition, we observed that the ESR contrast just to the right of the MoRe strip exceeded that just to the left of it (Fig. 2E), which indicated the excitation of additional, secondary spin waves by the MoRe strip itself. This enhanced excitation of secondary spin waves is presumably caused by an additional microwave current in the MoRe strip that is excited through the direct geometric inductive coupling with the gold microstrip when the MoRe impedance changes as it is cooled below T_c.

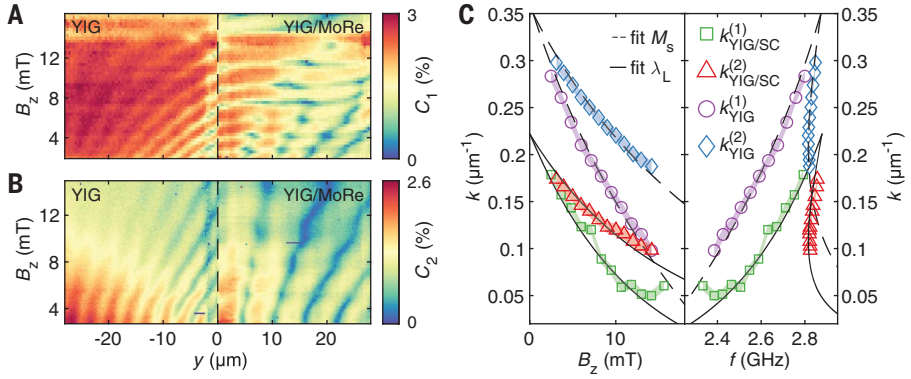

Fig. 3. Magnetic field dependence of the spin-wave dispersion in the magnet-superconductor hybrid. (**A** and **B**) Spatial line traces of the NV ESR contrasts C_1 and C_2 as a function of magnetic field B_z. Spin waves excited in the bare YIG region (y < 0) by the left Au microstrip (outside the imaged area) travel toward and then underneath the superconducting strip (y > 0), changing their wavelength. Interference with secondary spin waves excited at the MoRe strip edge (at y = 0) due to inductive coupling between Au and MoRe strips yields a beating pattern along B_z for y > 0. T = 5.5 K. The drive frequency is adjusted at each B_z to maintain resonance with the NV ESR transitions. (**C**) Spin-wave number as a function of field (left) and frequency (right), extracted from the data in (A) and (B) by means of Fourier transformation (fig. S2). The $k^{(i)}$ are the wave numbers measured with the field-aligned (i = 1) and misaligned (i = 2) NV ensembles. The error bars (indicated by shading) are determined by the inverse of the spatial sampling range in the y direction. We determined the saturation magnetization M_s by fitting the data in the bare YIG region, and the London penetration depth λ_L by fitting the data in the YIG-MoRe region using our YIG/SC model [supplementary text, section 2 (*19*)].

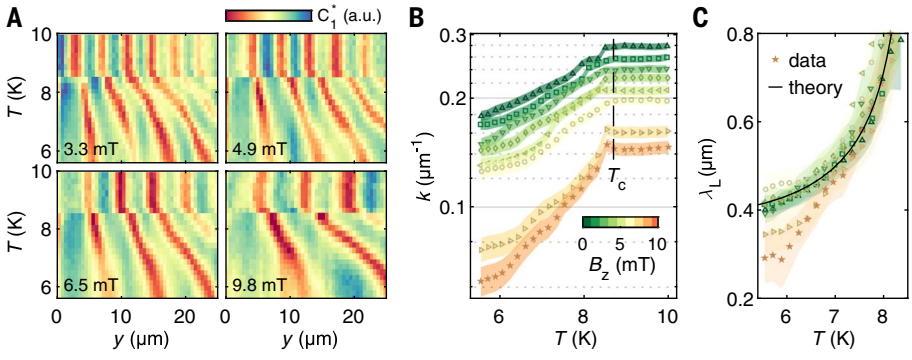

Fig. 4. Temperature tunability of the hybrid spin-wave–Meissner-current dispersion and extraction of the London penetration depth. (**A**) Spatial line traces of the NV ESR contrast C_1^* across the YIG-MoRe region as a function of temperature, showing the continuous change of the spin wavelength underneath the MoRe strip, for different in-plane magnetic fields B_z. The data are linearly detrended along y. Above the superconducting phase transition there is no temperature dependence of the wavelength, indicating the absence of the Meissner effect. A.u., arbitrary units. (**B**) Spin-wave numbers k extracted from data in (A) and from additional data in fig. S4 as a function of temperature. The colors indicate the different magnetic field values B_z. (**C**) London penetration depth λ_L of the MoRe film as a function of temperature, extracted from the data in (B) through our YIG/SC model. The black line represents the fit of the temperature dependence of $\lambda_L(T)$ from which we extracted T_c = 8.7 K and λ_L^0 = 380 nm. The colors indicate the different values of B_z as in (B).

Temperature- and field dependence of the spin-wave dispersion and extraction of the London penetration depth

We characterized the magnetic-field dependence of the spin-wave dispersion underneath the superconductor and used it to extract the London penetration depth λ_L at the T = 5.5 K base temperature of our cryostat. Spatial line traces of the NV ESR contrast across the strip shows the dependence of the spin wavelength on the applied magnetic field for the field-aligned (Fig. 3A) and misaligned (Fig. 3B) NV ensembles. In both measurements, we adjusted the drive frequency at each magnetic field to maintain resonance with the NV ESR frequency. We extracted the spin-wave numbers in the bare YIG and YIG-MoRe regions separately by Fourier transformation (fig. S2) and plotted these as a function of field and frequency in Fig. 3, C and D. A similar measurement with the bias field applied in plane along $\hat{x}$ shows that Meissner screening of the bias field does not play a significant role in the wavelength shift (fig. S3).

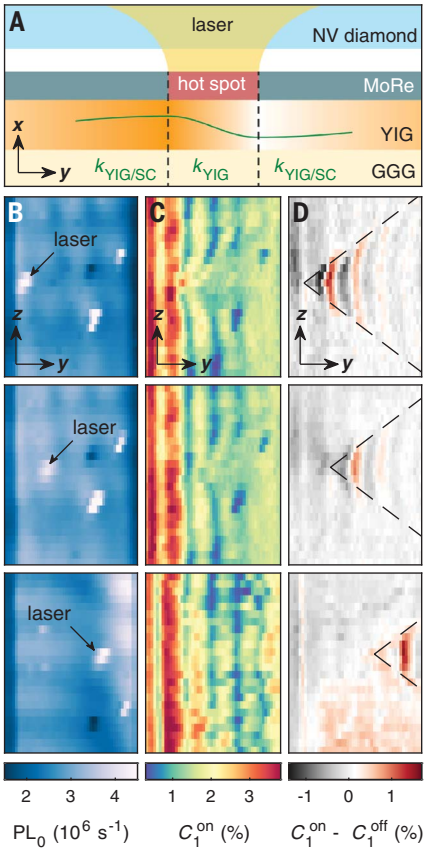

Fig. 5. Laser-induced spin-wave refraction at target locations. (**A**) Schematic illustration of a laser-induced scattering spot. By shining an auxiliary 594-nm laser on the sample, we created a hot spot in the MoRe strip that locally altered the effective refractive index governing the spin-wave propagation. (**B**) Scanning confocal microscope images of the NV photoluminescence at T = 5.5 K, with the auxiliary laser focused onto the MoRe strip at three different locations indicated by the arrows. Scale bar, 10 μm. (**C**) Spatial maps of the NV ESR contrast with auxiliary laser turned on (C_1^{on}) showing spin waves in the YIG-MoRe region that scatter on the laser spot. (**D**) Background-subtracted ESR contrast highlighting the laser-induced spin-wave scattering obtained by subtracting the ESR contrast with the auxiliary laser turned off C_1^{off} from the measurements in (C). B_z = 3.3 mT.

From the field dependence of the extracted spin-wave numbers in the bare YIG region, we extracted the YIG saturation magnetization M_s = 194(1) kA/m [supplementary text, section S2 (*19*)] in agreement with previous low-temperature measurements (*27*). We then used M_s as a fixed parameter to fit the field dependence of the spin-wave numbers underneath the superconducting strip using the hybridized YIG-MoRe spin-wave dispersion (Eq. 1). From this fit, we extracted a London penetration depth λ_L = 405(10) nm at T = 5.5 K, which agrees well with static-field nano–superconducting quantum interference device measurements (*28*).

The temperature dependence of the London penetration depth provides a powerful tool for tuning the spin wavelength. To demonstrate this, we imaged the spin waves in the YIG-MoRe region while sweeping through T_c at different magnetic fields (Fig. 4A and fig. S4). The extracted spin-wave number k is shown in Fig. 4B, with the color indicating the in-plane component of the magnetic field. We observed that k changes continuously with temperature over the superconducting phase transition in the YIG-MoRe region and remains unchanged in the bare YIG region (fig. S5). We did not observe global heating of the superconductor due to our excitation laser (fig. S6). Using our model, we extracted the London penetration depth $\lambda_L(T)$ for every observed value of k (Fig. 4C) [supplementary text, section S2 (*19*)]. We found that almost all data collapse onto a single curve described by $\lambda_L = \lambda_L^0[1-(T/T_c)^4]^{-1/2}$ (*29*), with T_c = 8.7 K and λ_L^0 = 380nm. The exceptions occurred when the spin wavelength $\lambda_{SW} = 2\pi/k$ became comparable to the width of the MoRe strip. Here, our approximation of the superconducting strip by an infinite film breaks down. These results highlight that imaging the hybridized spin-wave–Meissner-current transport modes is a powerful tool for extracting the temperature dependence of the London penetration depth.

Local control of spin-wave transport by laser-induced spin-wave refraction

Thus far, we have demonstrated dispersion engineering through global control of temperature and magnetic field. We now show that the creation of a hot spot in the superconductor with a focused laser enables local manipulation of the spin-wave transport by tuning the effective refractive index (Fig. 5A). To do so, we coupled an auxiliary, orange laser into our setup and focused it at target sites on the superconductor (Fig. 5B). The laser spot is visible through the locally enhanced NV photoluminescence. Spatial measurements of the NV ESR contrast C_1^{on} with the auxiliary laser on (Fig. 5C) show the spin-wave scattering patterns induced by the local hot spot. The reduction in amplitude behind the hot spot indicates destructive interference between the scattered and incident spin waves. Subtracting a reference measurement with the auxiliary laser turned off (Fig. 5D) highlights the angular profile of the scattered spin-wave patterns.

The characteristic "caustic" angles observed in these scattered patterns (dashed lines, Fig. 5D) result from the highly anisotropic dipolar spin-wave dispersion (*30*). Tracing the patterns to their origin shows that the scattering site is tightly confined to the laser location. Presumably, the laser locally breaks the superconductivity, inducing a local change in the magnetic environment seen by the spin waves, leading to local spin-wave refraction akin to defect-controlled spin-wave scattering (*30*). The ability to optically induce spin-wave refraction at target sites could be used to create devices such as gratings or magnonic crystals (*31*) and enable spin-wave manipulation through optical switching of flux-focusing regions in the superconducting strip.

Conclusions

We demonstrated local measurements of hybridized spin-wave–Meissner-current transport modes in a magnetic thin film equipped with a superconducting gate. The wavelength was tunable by temperature and field, enabling efficient phase-shifting of the spin-wavefronts and a notable in situ visualization and quantitative extraction of the London penetration depth as a function of temperature. Because MoRe is a type-2 superconductor with an estimated lower critical field of $H_{c1} = \frac{\Phi_0}{4\pi\lambda_L^2}\left[\ln\left(\frac{\lambda_L}{\xi}\right)+0.5\right] \approx$ 4 mT at $T \approx 5$ K (*32*, *33*), where $\xi \approx 0.01$ μm is the coherence length (*34*) and Φ_0 the superconducting flux quantum, Abrikosov vortices were expected in measurements such as those in Fig. 3B with a few-mT out-of-plane field component. However, we did not identify vortex-related effects in these measurements, which look qualitatively similar to those with purely in-plane field (fig. S3). Presumably, the presence and location of vortices is strongly influenced by our focused excitation laser, as highlighted by recent magneto-optical (*35*) and wide-field NV-imaging experiments (*36*). In particular, (*35*) showed that vortices can be annihilated by the laser through local heating above T_c or pushed by the laser to new pinning sites or border regions of the superconductor. The presented microwave magnetic imaging of the spin-wave transport modes in a YIG-MoRe heterostructure shows the versatility of superconducting gates for spin-wave manipulation, enables determining the temperature-dependent London penetration depth, and opens new opportunities for creating wave-based circuit elements such as filters, mirrors, and cavities.

REFERENCES AND NOTES

1. S. A. Wolf *et al.*, *Science* **294**, 1488–1495 (2001).
2. A. V. Chumak, V. I. Vasyuchka, A. A. Serga, B. Hillebrands, *Nat. Phys.* **11**, 453–461 (2015).
3. A. Barman *et al.*, *J. Phys. Condens. Matter* **33**, 413001 (2021).
4. J. Sinova, S. O. Valenzuela, J. Wunderlich, C. H. Back, T. Jungwirth, *Rev. Mod. Phys.* **87**, 1213–1260 (2015).
5. L. J. Cornelissen, J. Liu, R. A. Duine, J. Ben Youssef, B. J. Van Wees, *Nat. Phys.* **11**, 1022–1026 (2015).
6. A. Hamadeh *et al.*, *Phys. Rev. Lett.* **113**, 197203 (2014).
7. T. Yu, C. Liu, H. Yu, Y. M. Blanter, G. E. W. Bauer, *Phys. Rev. B* **99**, 134424 (2019).
8. J. Chen *et al.*, *Phys. Rev. Lett.* **120**, 217202 (2018).
9. Y. Sun *et al.*, *Phys. Rev. Lett.* **111**, 106601 (2013).
10. I. Bertelli *et al.*, *Adv. Quantum Technol.* **4**, 2100094 (2021).
11. Z. Y. Zhang *et al.*, *Supercond. Sci. Technol.* **25**, 025009 (2012).
12. A. Blais, A. L. Grimsmo, S. M. Girvin, A. Wallraff, *Rev. Mod. Phys.* **93**, 025005 (2021).

13. I. A. Golovchanskiy *et al*., *J. Appl. Phys.* **127**, 093903 (2020).
14. O. V. Dobrovolskiy *et al*., *Nat. Phys.* **15**, 477–482 (2019).
15. T. Yu, G. E. W. Bauer, *Phys. Rev. Lett.* **129**, 117201 (2022).
16. L. Rondin *et al*., *Rep. Prog. Phys.* **77**, 056503 (2014).
17. T. X. Zhou *et al*., *Proc. Natl. Acad. Sci. U.S.A.* **118**, e2019473118 (2021).
18. I. Bertelli *et al*., *Sci. Adv.* **6**, eabd3556 (2020).
19. Materials and methods, and supplementary text, figures and references are available as supplementary materials.
20. F. Casola, T. Van Der Sar, A. Yacoby, *Nat. Rev. Mater.* **3**, 17088 (2018).
21. R. Schirhagl, K. Chang, M. Loretz, C. L. Degen, *Annu. Rev. Phys. Chem.* **65**, 83–105 (2014).
22. D. R. Glenn *et al*., *Geochem. Geophys. Geosyst.* **18**, 3254–3267 (2017).
23. P. Andrich *et al*., *npj Quantum Inf.* **3**, 28 (2017).
24. C. S. Wolfe *et al*., *Phys. Rev. B Condens. Matter Mater. Phys.* **89**, 180406 (2014).
25. A. G. Gurevich, G. A. Melkov, *Magnetization Oscillations and Waves* (CRC Press, 1996).
26. S. R. Seshadri, *Proc. IEEE* **58**, 506–507 (1970).
27. S. Knauer *et al*., *J. Appl. Phys.* **133**, 143905 (2023).
28. A. G. Shishkin *et al*., *Supercond. Sci. Technol.* **33**, 065005 (2020).
29. M. Tinkham, *Introduction to superconductivity* (Dover Publications, 2nd edition, 2004).
30. R. Gieniusz *et al*., *Appl. Phys. Lett.* **102**, 102409 (2013).
31. A. V. Chumak, A. A. Serga, B. Hillebrands, *J. Phys. D Appl. Phys.* **50**, 244001 (2017).
32. W.-K. Kwok *et al*., *Rep. Prog. Phys.* **79**, 116501 (2016).
33. V. E. Calado *et al*., *Nat. Nanotechnol.* **10**, 761–764 (2015).
34. K. Makise *et al*., *Mater. Res. Express* **5**, 096406 (2018).
35. I. S. Veshchunov *et al*., *Nat. Commun.* **7**, 12801 (2016).
36. S. E. Lillie *et al*., *Nano Lett.* **20**, 1855–1861 (2020).
37. M. Borst *et al*., Data for: Observation and control of hybrid spin-wave–Meissner-current transport modes, version 1, Zenodo (2023).

ACKNOWLEDGMENTS

We thank A. F. Otte for commenting on the manuscript and T. Yu and G.E.W. Bauer for discussions. **Funding:** This work was supported by the Dutch Research Council (NWO) under awards VI.Vidi.193.077, NGF.1582.22.018, and OCENW.XL21.XL21.058. This work was also supported by the Dutch National Growth Fund (NGF) as part of the Quantum Delta NL programme. **Author contributions:** Conceptualization: T.S. and M.B.; Sample design and fabrication: M.B.; Diamond membrane fabrication: B.S. and M.B.; Membrane placement: A.L. and S.K.; Constructing experimental setup: M.B. and A.L.; Measurements and software: M.B., P.H.V., A.L., and I.B.; Data analysis: M.B., P.H.V., and A.T.; Theory: T.S. and Y.M.B.; Figures: M.B. and P.H.V.; Funding acquisition: T.S.; Project administration: M.B. and T.S.; Supervision: T.S. and M.B.; Writing – original draft: M.B., T.S., and P.H.V.; Writing – review and editing: M.B., T.S., P.H.V., and Y.M.B. **Competing interests:** The authors declare that they have no competing interests. **Data and materials availability:** All data presented in this work are available at Zenodo (*37*).

SUPPLEMENTARY MATERIALS

science.org/doi/10.1126/science.adj7576
Materials and Methods
Supplementary Text
Figs. S1 to S6
References (*38*–*42*)

Submitted 14 July 2023; accepted 18 September 2023
10.1126/science.adj7576

Observation and control of hybrid spin-wave–Meissner-current transport modes

M. Borst, P. H. Vree, A. Lowther, A. Teepe, S. Kurdi, I. Bertelli, B. G. Simon, Y. M. Blanter, and T. van der Sar

Science **382** (6669), . DOI: 10.1126/science.adj7576

Editor's summary

The ability to control spin and charge transport on a chip has revolutionized information technology. For spintronics, the collective spin excitations of magnetic materials, known as spin-waves, have emerged as a promising platform that can offer new functionalities because of their wave nature. However, control of the spin-waves has remained a formidable challenge. Borst *et al*. show that the diamagnetism of a superconductor can be used to shape the magnetic environment that governs the transport of spin-waves in a magnetic thin film. Magnetic imaging showed how the diamagnetism leads to spin-waves with strongly altered, temperature-tunable wavelengths. Control of spin-wave transport using the diamagnetic response of a superconducting gate will be important for developing device applications. —Ian S. Osborne